RSC Applied Interfaces

ROYAL SOCIETY OF CHEMISTRY

PAPER

View Article Online
View Journal | View Issue

Check for updates

Cite this: *RSC Appl. Interfaces*, 2025, **2**, 82

Influence of surface roughness and metal oxide nanoparticles on airframe with icephobic coatings†

Kate Yeadon,[ab] Edward P. C. Lai,*[a] Xiao Huang[b] and Naiheng Song[c]

Received 1st August 2024,
Accepted 23rd September 2024

DOI: 10.1039/d4lf00279b

rsc.li/RSCApplInter

Icephobic coatings represent a sustainable and cost-efficient technology for preventing hazardous ice buildup across airframe surfaces. However, commercially available icephobic coatings still lack the metrics required for aircraft applications. Cyclic voltammetry is an electrochemical analysis technique that can detect ice formation by providing a distinct oxidation current response to the phase change. In this study, the technique was used to compare individual surface temperatures at water freezing across a variety of icephobic coatings on airframe surfaces that were roughened by sand blasting with alumina and modified by zinc oxide or neodymium oxide nanoparticles. The effect of sand blasting alone on delayed water freezing was marginal due to the self-leveling properties of icephobic coatings. However, addition of metal oxide nanoparticles delayed the formation of ice on the icephobic coatings. These findings provide new insight into the mechanism governing freezing point shift for the benefit of aircraft flying under extreme weather conditions.

Introduction

Icing and ice adhesion on aircraft surfaces are major sources of safety hazards and equipment malfunctions.[1–5] Aircraft flying under extreme weather conditions incur ice accretion through the accumulation of impinging precipitation, which freezes upon contact with the aircraft or after rolling across the forward-facing surface.[6,7] The accumulation of ice on critical aircraft surfaces, such as wings, propellers, fuselage, engine nacelles, airfoils, and sensor ports, can substantially interfere with the operation of the aircraft.[8] Grounded aircraft are also susceptible to the accumulation of ice, frost, or snow on the airframe which, if not removed, can significantly impact aircraft control and stability during take-off. The breadth and severity of this problem have demanded the development of new, cost-effective, energy-efficient, and environmentally sustainable solutions to combat the threat of icing against the aerospace and aviation industries.

Icephobic coatings offer a promising passive technology to delay and reduce ice accretion on airframe surfaces.[9–12] The icephobicity of a coating can be assessed through material characteristics such as water contact angles, water freezing temperature, and ice adhesion strength.[13] In comparison with active ice protection systems currently used in the aerospace industry, icephobic coatings present several merits including lower costs, reduced energy requirements, mechanical durability for many de-icing cycles, and negligible environmental impact. As such, a large body of literature has been published to study and develop different types of icephobic coatings, including superhydrophobic,[14–18] liquid-infused,[19,20] hydrated surfaces,[21] and solid lubricant film[22] to minimize or even eliminate the need for complex and costly active ice protection systems. However, despite significant progress, the development of icephobic coatings exhibiting both high icephobicity and robustness required for aerospace applications remains a challenge. To date, a commercial icephobic coating viable for aircraft applications has yet to be established.

Given the aerospace industry's strong need for effective passive ice protection, it is worthwhile to explore how the icephobicity of existing coatings can be further enhanced through surface modifications. In this study, we will investigate two such modifications: increasing surface roughness and depositing metal oxide nanoparticles onto the coating surface. Surface roughness is one of two main factors, along with wettability, responsible for determining the probability of ice formation.[23] Ice adhesion strength can be drastically reduced by increasing the number of air pockets at the ice–solid interface to lower liquid–solid contact prior to freezing.[24,25] This patterning can be achieved by

[a] *Department of Chemistry, Carleton University, 1125 Colonel By Dr., Ottawa, ON, K1S 5B6, Canada. E-mail: edwardlai@cunet.carleton.ca*
[b] *Department of Mechanical and Aerospace Engineering, Carleton University, 1125 Colonel By Dr., Ottawa, ON, K1S 5B6, Canada*
[c] *Aerospace Research Centre, National Research Council of Canada, 1200 Montreal Rd., Ottawa, ON, K1A 0R6, Canada*

† Electronic supplementary information (ESI) available. See DOI: https://doi.org/10.1039/d4lf00279b

preparing surfaces at roughness levels close to or smaller than critical ice nuclei size, thereby reducing ice formation through the elimination or significant delay of ice nucleation.[26] Surface roughness is not sufficient enough to lower ice adhesion independently. Instead, surface materials of similar roughness have shown a strong dependence on surface energy, such that lower surface temperatures at water freezing were associated with lower surface energies.[27,28] This correlation has shown that the surface temperature at ice formation can be significantly reduced by adjusting surface roughness to maximize the free energy barrier.[29,30]

Surfaces roughened with micro- or nano-structures have also shown reduced ice adhesion strengths and lower surface temperatures at ice nucleation.[31] For example, silica nanoparticles were added to selected icephobic coatings to reduce ice formation on the surface.[32] Nanoparticles offer corrosion protection, wear-resistance, and thermal protection, which are areas within the aerospace industry where existing icephobic coatings lack performance. Several other nanomaterials, such as graphene-based composites,[33,34] carbon nanotubes,[35] and metal oxide nanoparticles,[36] are already being developed to prevent ice accumulation on aircraft surfaces while simultaneously reducing corrosion, erosion, and fuel usage.[37] Similarly, these particles are being grown on existing icephobic surfaces to generate micro- and nano-scale roughness.[38] Indeed, increased surface roughness and nanoparticle deposition have both been found to delay ice formation on coated surfaces.

Cyclic voltammetry has been extensively used to study electrochemical processes at temperatures well below a solvent's freezing point.[39–47] It has also been used as an analytical technique to detect ice formation on a variety of surfaces, with and without icephobic coatings, in previous studies conducted by this research group. A significant increase of faradaic current density was observed across all sample surfaces during the water to ice phase change using this technique, which suggests that it can be used as a sensing technique for ice formation.[48] Icing research has extended to the development of technologies designed to detect ice formation on grounded and in-flight aircraft.[49] Vibrating probes,[50] optical/particle beam occlusion,[51] and rotating cylinder/torque measurement detectors[52] exist for in-flight detection of ice accretion. However, these systems have yet to be widely implemented within the aerospace industry for active control of ice protection. Due to the need for accurate ice detection of aircraft surfaces, reliable sensing technologies, such as cyclic voltammetry, show promise as a new option for sensing early icing.

The objective of this work is to determine the surface freezing temperature of icephobic coatings using cyclic voltammetry after increasing surface roughness and depositing metal oxide nanoparticles on the surface. This method was used to compare the surface temperature at the point of water freezing to note any differences in delaying ice formation. The surfaces of aluminum alloy coupons were roughened by sand blasting with alumina. Zinc oxide or neodymium oxide nanoparticles were then added to selected icephobic liquid coatings and applied to the surface. By using cyclic voltammetry, the impact of these modifications on surface freezing temperature was studied. Both increased surface roughness and the deposition of metal oxide nanoparticles reduced the surface temperature required for ice formation. This paper will determine whether this relationship persists over a variety of icephobic coatings, thereby supporting the use of the developed cyclic voltammetry technique as a sensor for surface icing for improving the anti-icing perseverance of aircrafts and actuating the ice protection system of an aircraft in flight.

Materials and experimental methods

Sample preparation

Six smooth and six roughened aluminum alloy (AA 2024-T3, 100 mm × 26 mm × 1.2 mm) coupons were used as the substrates. The aluminum coupons were cleaned with soap water, wiped with isopropyl alcohol, and air dried before applying icephobic coatings. Five commercial icephobic coatings were evaluated: Nusil® R-1009 RTV silicone dispersion (Avantor Sciences, Radnor, PA, USA), Nusil® R-2180 silicone dispersion (Avantor Sciences, Radnor, PA, USA), Sylgard™ 184 silicone elastomer (Dow Chemical, Midland, MI, USA), Liquid Glass Shield Hard Surface (Liquid Glass Shield, London, UK), and MG Chemicals® Silicone Conformal Coating (MG Chemicals, Burlington, ON, Canada). These coatings were selected due to their commercial availability and the variance in their physicochemical properties pertaining to icing. The coating application followed the recommended protocols as per the technical data sheets.[53–57] Relevant physical and chemical properties of the coatings are summarized in Table 1. Coating thickness (t) was estimated through dividing the mass of dry coating by the coated area and the coating density.

Surface roughing and roughness measurement

Roughening of AA 2024-T3 coupon surfaces was achieved by sandblasting with 430 micron Al_2O_3 (alumina) under the following conditions: 50 psi, 4 passes at a 6″ blasting distance and a 90° blasting angle. The nozzle size was ¼″ in diameter. The surface profile of both smooth and roughened coupons was measured using a Bruker DektakXT surface profilometer (Billerica, MA, USA) with a resolution of 4 Å. A 2000 micron rectilinear profile reading was taken in one direction across the surface. Surface roughness (Rz) was calculated as the difference between the highest peak and the deepest undercut measured; it was meant for indicating the magnitude of thickness variations. These measurements were repeated at six locations across the sample surface and averaged. This process was repeated after the icephobic coatings were applied to determine the impact of coating on the surface roughness of each coupon.

Table 1 Properties of commercial icephobic coatings applied to the smooth and roughened AA 2024-T3 coupons

Coating	Description	Viscosity (mPa s)	Dry film density (g cm^{-3})	Coating thickness (mm)	
				Smooth coupon	Rough coupon
Nusil® R-1009	One-part RTV silicone rubber protective and conformal coating	6150	0.82	0.36	0.33
Nusil® R-2180	Two-part silicone elastomeric icephobic coating	3075	0.96	0.34	0.35
Sylgard™ 184	Two-part silicone elastomeric coating	555	1.11	0.28	0.31
Liquid Glass Shield	Protective nano coating	Not provided	1.00	0.07	0.07
MG Silicone	Silicone modified aerosol conformal coating	<18.2	0.89	0.09	0.10

Surface modification with metal oxide nanoparticles

Icephobic coatings comprising metal oxide nanoparticles were prepared and investigated for their surface temperatures at water freezing. Specifically, 0.1 g of zinc oxide (ZnO) nanoparticles or neodymium oxide (Nd_2O_3) nanoparticles (Sigma-Aldrich, St. Louis, MO, USA) were added to 20 mL of the icephobic coatings and sonicated for 20 minutes using the FS-300N Ultrasonic Homogenizer Sonicator Processor to ensure the uniform dispersion of the nanoparticles throughout the coating. The ZnO or Nd_2O_3 modified coating was then applied to a cleaned AA 2024-T3 coupon and cured following the protocols outlined in the hydrophobic coating technical datasheets.

Water contact angle measurement

The water contact angle was measured by the sessile drop method using an automated ramé-hart Instruments 290-U4 goniometer (Succasunna, NJ, USA). Static contact angles were measured by lowering a drop of de-ionized water (*ca.* 4 μL) at 4 different locations on each test surface using the instrument's automated dispensing system. Dynamic contact angles (*i.e.*, advancing and receding) were measured using the volume addition and subtraction method. The advancing contact angle was measured by keeping the addition of de-ionized water in 0.25 μL steps to the water droplet until the maximum contact angle was observed. The contact angle measurement had a 0.5 s delay time. Inversely, the receding contact angle was measured by subtracting the water droplet in 0.25 μL steps until its edges started retracting up or a minimum contact angle was reached. The advancing and receding contact angle measurements were repeated 4 times on each test surface. All contact angles were analyzed by the DROPimage Advanced software.[58]

Icing set-up

Water freezing temperatures on different test surfaces were analyzed using a cyclic voltammetric (CV) technique in a home-built icing chamber (Fig. 1) that provides a temperature- and moisture-controlled environment suitable for icing. An ATS-CP-1002 cold plate (Advanced Thermal Solutions, Norwood, MA, USA) was connected to an MGW Lauda Brinkmann RM 3 water bath cooler (Marlton, NJ, USA)

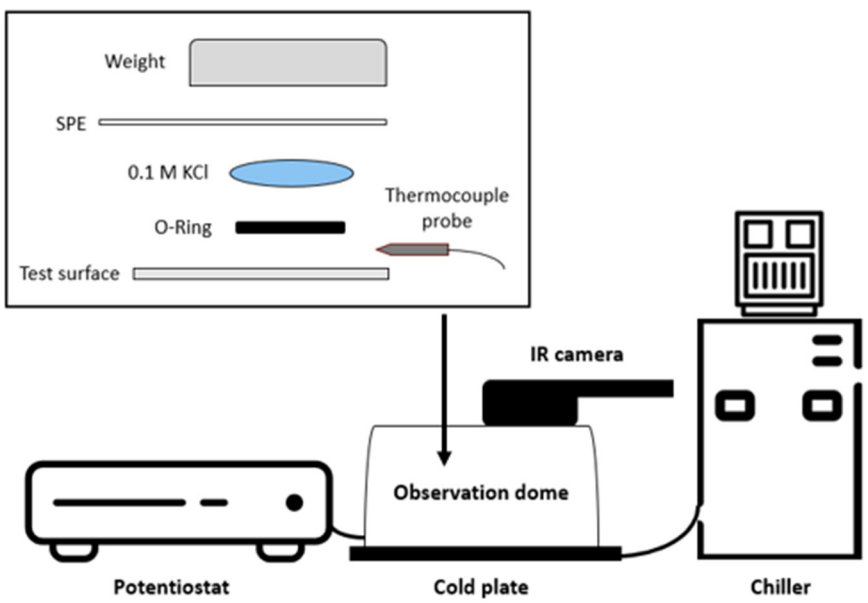

Fig. 1 Schematics of the icing set-up constructed for cyclic voltammetry analysis of 0.1 M KCl solution from room temperature to individual surface temperatures at water freezing.

that was used to regulate the cold plate temperature. Nitrogen gas was pumped through the icing chamber in a steady stream to regulate moisture. It was assumed that the relative humidity in the icing chamber was very low due to the purging nitrogen gas flow and no condensation could occur inside the chamber during testing. However, no humidity level was actually measured. During the test, an aluminum coupon was placed on the cold plate in the icing chamber with the test surface facing upwards. Every effort was made to ensure complete contact between the sample coupon and the cold plate to achieve an equal temperature distribution. A Digi-Sense® thermocouple probe was thermally insulated and mechanically taped to the test surface of the coupon to provide accurate surface temperature measurements. A 150 μL droplet of water containing 0.1 M KCl electrolyte was placed on the coupon surface within a rubber O-ring (7/16″ inner diameter and 9/16″ outer diameter). A screen-printed electrode (SPE) was placed on top of the O-ring in direct contact with the water droplet contained within the O-ring and the screen-printed electrode was then connected to a Solartron Analytical SI 1287 potentiostat (Farnborough, Hampshire, UK) in a three-electrode configuration (*i.e.*, a graphite working electrode, an Ag/AgCl reference electrode, and a graphite counter electrode). The SPE and O-ring were secured in place using a 200 g weight that compressed the water drop into a columnar shape under constant pressure at all temperatures. Upon freezing, slight volume expansion is expected but was not considered critical in this study at this stage. The working electrode potential was scanned between +1.0 and −1.0 V with an initial potential of zero volts relative to the reference electrode. During this analysis, the temperature of the cold plate was slowly decreased at a cooling rate of 0.2 °C min^{-1} to allow the water droplet on the coupon surface to freeze. Cyclic voltammograms were collected continuously at a 100 mV s^{-1} scan rate until the phase change from water to ice was observed by a sharp increase in the faradaic current density at +1.0 V. The resulting voltammetric responses were analyzed to determine whether the modification of test surfaces influenced their temperature at water freezing. Surface temperatures could be verified by a visual observation on the phase change using a Reed Instruments R2160 thermal imaging camera (Wilmington, NC, USA) mounted on top of the icing chamber.

Results

Surface roughness

The measured surface roughness for each test coupon with and without coating is summarized in Fig. 2. As expected, the uncoated, sandblasted AA 2024-T3 coupons (Rz = 1.3–2.4 μm) exhibited greater surface roughness than the smooth aluminum coupons (Rz = 0.4–0.6 μm). The application of coatings to the coupon surface reduced the roughness of all coupon surfaces, due to the self-levelling ability of the coatings and the higher coating thickness compared to the surface roughness of the substrate AA 2024-T3 coupons, regardless of the surface roughening.

As it can be seen from Fig. 2, all the silicone coated coupons (*i.e.*, by Nusil® R-1009, Nusil® R-2180 and Sylgard™ 184) showed comparably small roughness variation of less than 0.365 μm, independent of the surface roughness of the substrates. In contrast, Liquid Glass Shield and MG Silicone coated coupons showed greater surface roughness on the roughened aluminum substrates than on the smooth substrates; the measured roughness differences are 0.4 μm and 0.6 μm, respectively. The Liquid Glass Shield and MG Silicone coatings maintained much thinner dry film thickness than the silicone coatings (Table 1). As such, their self-leveling properties are more variable across coupons with increased surface roughness.

Water contact angles

The measured static (θ), advancing (θ_{adv}) and receding (θ_{rec}) contact angles for all coated and uncoated coupons are summarized in Table 2. The bare aluminum exhibited static water contact angles of *ca.* 93° for the smooth coupons and *ca.* 99° for the roughened coupons. The application of the

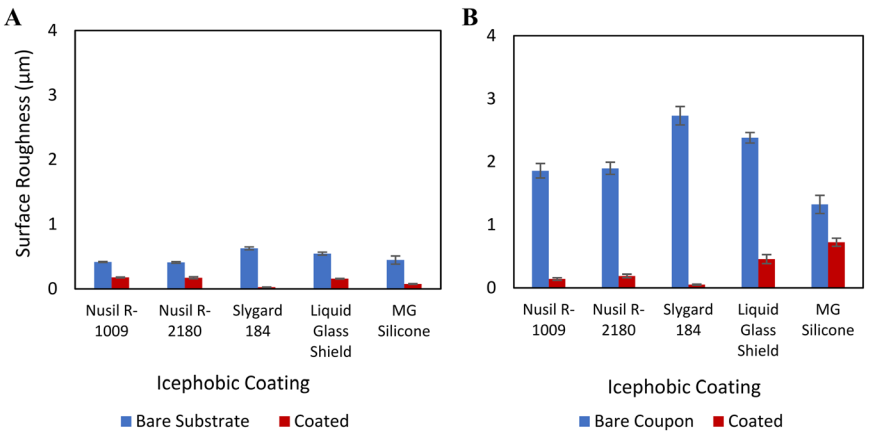

Fig. 2 Averaged surface roughness measurements for AA 2024-T3 coupons on: (A) smooth substrates and (B) rough substrates.

Table 2 Averaged water contact angles for AA 2024-T3 coupons, with standard errors (= standard deviation/$\sqrt{\text{number of samples}}$)

	Smooth substrate				Roughened substrate			
Coating	Static contact angle (θ, °)	Advancing contact angle (θ_{adv}, °)	Receding contact angle (θ_{rec}, °)	Hysteresis ($\Delta\theta$)	Static contact angle (θ, °)	Advancing contact angle (θ_{adv}, °)	Receding contact angle (θ_{rec}, °)	Hysteresis ($\Delta\theta$)
Uncoated	93.6 ± 0.5	94.0 ± 1.6	35.9 ± 1.7	58.1	99.0 ± 1.1	97.7 ± 0.7	48.6 ± 2.7	49.1
Nusil® R-1009	117.9 ± 0.6	124.5 ± 0.8	53.6 ± 2.8	70.9	114.7 ± 1.1	117.6 ± 0.8	80.7 ± 1.0	36.9
Nusil® R-2180	105.3 ± 1.8	107.1 ± 0.9	66.5 ± 1.0	40.6	112.6 ± 0.4	116.4 ± 0.4	74.5 ± 1.0	41.9
Sylgard™ 184	108.3 ± 1.0	106.8 ± 0.4	74.1 ± 1.2	32.7	111.9 ± 0.8	116.7 ± 1.5	74.8 ± 1.6	41.9
Liquid Glass Shield	96.2 ± 0.7	103.7 ± 0.7	85.0 ± 2.1	18.7	96.4 ± 1.1	103.2 ± 0.8	76.3 ± 1.5	26.9
MG Silicone	91.6 ± 0.3	93.0 ± 0.4	61.3 ± 1.5	31.7	85.1 ± 0.3	96.3 ± 2.6	52.1 ± 1.1	44.2

icephobic coatings was anticipated to increase the hydrophobicity of the aluminum substrate, which was confirmed for all the test coupons except for the MG Silicone-coated ones that showed slightly lower static water contact angles of *ca.* 92° for the smooth substrate and 85° for the roughened substrate (Fig. 3 and Table 2).

While static contact angles characterize a surface, the receding contact angle, a dynamic property, is known to have an established relationship with the ice adhesion strength.[59] No clear correlation of the receding angle with freezing temperature was observed from the data in this study. Fundamentally, ice adhesion strength and water freezing temperature are two distinct parameters governed by different surface properties. More research will be needed to investigate this correlation in future studies. As shown in Table 2, all the coated coupons recorded noticeably higher receding contact angles than the uncoated coupons, including the MG Silicone coated coupons. This suggests an increased icephobicity due to the coating application. Trends among the receding contact angles of the studied coatings were consistent across both the smooth and roughened AA 2024-T3 substrates. Additionally, the rough substrate-based coupons recorded higher receding contact angles in all cases than those based on smooth substrates, with increases being as much as 27.1°. This result was anticipated as the Wenzel equation establishes a relationship between the surface roughness and water contact angle.[60] As such, the apparent contact angle is expected to increase with the roughening of a hydrophobic (*i.e.*, contact angle >90°) surface.[61] The roughened substrate-based coupons all possess greater surface roughness than the smooth substrate-based coupons. Therefore, on the basis of this criterion, it was not surprising that the rough coupons displayed greater water contact angles (both static and dynamic) than the smooth coupons. The receding contact angle is influenced by surface roughness but predicting it directly using the Wenzel equation is not straight forward.[62]

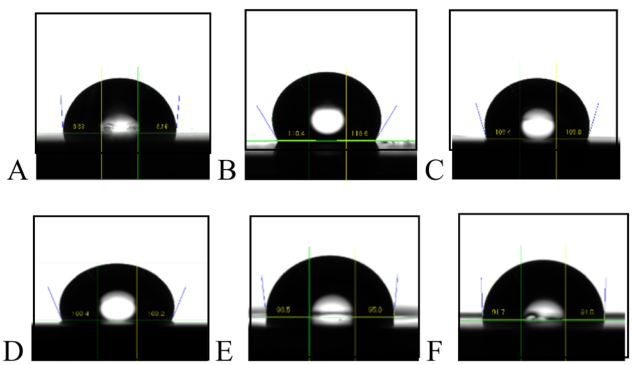

Fig. 3 Water droplet profiles on smooth AA 2024-T3 with and without coating: (A) uncoated, (B) Nusil® R-1009, (C) Nusil® R-2180, (D) Sylgard™ 184, (E) Liquid Glass Shield, and (F) MG Silicone.

Freezing temperature determination using CV analysis

CV analysis has been demonstrated as an effective technique for detecting the freezing of water on a surface with a high degree of accuracy. In this study, the CV technique was employed to measure the surface temperature of all the test samples upon water freezing. As anticipated, the freezing temperature of water appeared to vary between the coated coupons as the icing behaviour is influenced by the surface properties, where a delayed nuclei formation due to surface hydrophobicity can lead to supercooling of water and decreased freezing temperature. In our study, all the coupons recorded freezing temperatures below 0 °C (*i.e.*, the freezing point of water under equilibrium conditions) when the water–ice phase change was observed. The depression of freezing temperature by about 0.37 °C caused by the use of 0.1 M KCl as the supporting electrolyte in the CV analysis was accounted for in the interpretation of the experimental data. The corrected freezing point temperatures on different test surfaces are presented in Table 3.

The smooth uncoated smooth AA 2024-T3 coupon exhibited the highest surface temperature of −1.2 °C at water

Table 3 Surface temperatures on the AA 2024-T3 coupons at the freezing of a 150 μL water after adjustment of 0.1 M KCl freezing point depression

	Surface temperature (±0.2 °C)	
Coating	Smooth substrate	Roughened substrate
Uncoated	−1.2	−1.6
Nusil® R-1009	−3.4	−3.7
Nusil® R-2180	−2.7	−2.8
Sylgard™ 184	−4.3	−4.5
Liquid Glass Shield	−3.7	−3.8
MG Silicone	−3.9	−4.1

freezing, followed by the roughened uncoated AA 2024-T3 coupon, which showed a freezing temperature of −1.4 °C. In contrast, the coated coupons exhibited freezing temperatures lower than the uncoated ones, ranging from a temperature decrease of 1.5 °C for Nusil® R-2180 to 3.1 °C for Sylgard™ 184. Little difference in freezing temperature was observed between the coated coupons with smooth and roughened substrates. This result could be expected as a decrease in the temperature required for water freezing had previously been shown to not be significantly affected by surface topography.[63]

Influence of metal oxide nanoparticles

The selected coatings were modified with the addition of ZnO and Nd_2O_3 nanoparticles to investigate the effect of the presence of metal oxide nanoparticles on the water freezing temperature. ZnO nanoparticles have been shown to increase the icephobicity of surfaces,[64,65] while Nd_2O_3 nanoparticles, a rare-earth oxide with intrinsic hydrophobicity, were investigated for similar icephobicity enhancement.[66,67] As such, CV analysis of water freezing temperatures of the modified surfaces was carried out. As with the coupons studied above, all the metal oxide nanoparticle-modified coatings showed a significant spike in the faradaic current density at +1.0 V *versus* Ag/AgCl at the water freezing temperature. The resulting changes in the averaged surface temperature at water freezing are displayed in Fig. 4.

The presence of ZnO or Nd_2O_3 nanoparticles on the surface of bare AA 2024-T3 coupons and in the coatings deposited on smooth and roughened AA 2024-T3 substrates was found to decrease the water freezing temperatures. This decrease was most significant with ZnO nanoparticles which lowered the surface temperature at water freezing by 0.9 °C. Nd_2O_3 nanoparticles on AA 2024-T3 or in the coatings also resulted in a water freezing temperature decrease by 0.1–0.6 °C. As a decrease in surface temperature of ice formation is a metric of icephobicity, it can thus be concluded that the presence of these metal oxide nanoparticles on the coupon surfaces increases the icephobicity. These findings corroborate the known ability of ZnO nanoparticles to enhance the anti-icing properties and confirm the hypothesis that similar anti-icing properties can be attributed to Nd_2O_3 nanoparticles. As shown in Fig. 4, little difference in water freezing temperature was observed between the smooth and roughened aluminum coupons. Furthermore, the coated coupons exhibited a further decrease in the surface temperature at water freezing compared with the uncoated coupons, with uncoated AA 2024-T3 displaying the highest surface temperature at water freezing (−2.1 °C and −2.5 °C for ZnO nanoparticles on the smooth/rough coupons, and −1.8 °C and −2.2 °C for Nd_2O_3 nanoparticles).

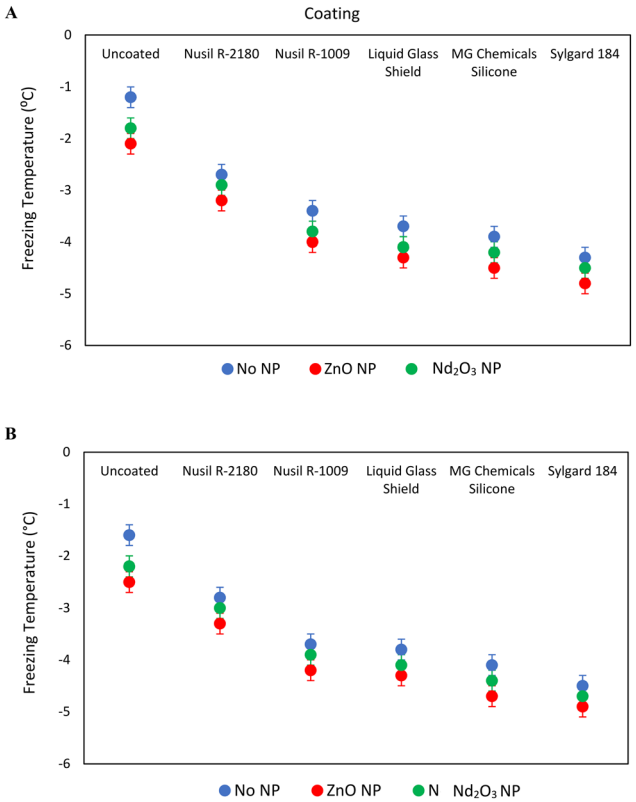

Fig. 4 Freezing temperature comparison of a 150 μL water droplet on various coatings comprising ZnO and Nd_2O_3 nanoparticles on: (A) smooth and (B) roughened AA 2024-T3 substrates.

Discussion

Water freezing on surfaces of AA 2024-T3 coupons that are smooth, roughened by sandblasting, or modified by various coatings with or without metal oxide nanoparticles was investigated by a cyclic voltammetric sensing technique, in relation to the icephobic properties of the surfaces. This versatile electrochemical analysis technique can be used to investigate the redox behavior of chemical species over a range of electrical potential. Voltammetry measures the redox current at different applied potentials by ramping the working electrode potential linearly over time, most notably the loss of electrons (*i.e.*, oxidation) or gain of electrons (*i.e.*, reduction). In the measured water droplets, the oxidation current was produced by Cl^- ions following this chemical half equation: $2Cl^- \rightarrow Cl_{2(g)} + 2e^-$. Supporting electrolyte ions could move freely through water above its freezing point under the control of diffusion down a concentration gradient. The liquid-to-solid phase change was expected to switch the dominant mass transfer mechanism within the water droplet from diffusion to a surface-confined pathway. The Cl^- ions were concentrated at the electrode surface as water froze necessitating a surface-confined process. Presumably, the layer of water near the cold plate surface froze first, thereby pushing the Cl^- ions upwards out of the ice crystals. As a result, the upper layer of the water droplet saw a gradual increase in Cl^- concentration as icing spreads. The concentration of Cl^- ions increased at the SPE surface as ice formation continued, ending with the highest current (or rate of electron transfer) being recorded at the freezing point of

water. In addition, the mobility of Cl^- ions changed at the freezing point. Cyclic voltammetric scans did show a very distinct rise in the current density at +1.0 V, *versus* Ag/AgCl, upon water freezing on all coupons. Surface roughness was not found to significantly influence the water freezing temperature on the coated surfaces, whereas the addition of metal oxide nanoparticles, *i.e.*, ZnO and Nd_2O_3 nanoparticles, in the coatings reduced the observed surface temperature at water freezing, and therefore, increased the icephobicity of modified surfaces.

Influence of roughness on water freezing temperature

The application of coatings to the AA 2024-T3 coupons consistently reduced their surface roughness. As such, the resulting difference in water freezing temperature was insignificant between the smooth and rough coupons (Fig. 5), not exceeding the measurement uncertainty (±0.2 °C). These results suggest that roughening the coupon surfaces (original roughness = 0.4–0.6 μm) by sandblasting (final roughness = 1.8–2.4 μm) did not substantially contribute to a decrease in surface temperature at ice formation. It had previously been shown that the surface roughening at the microscale level can result in a superhydrophobic surface (water contact angle > 150°), which was found to achieve notably lower water freezing times.[68,69] However, the water contact angles obtained from the prepared samples demonstrated that the roughness of test surfaces was not comparable to superhydrophobic materials (*i.e.*, surface patterning smaller than critical ice nuclei size). Although substrate roughness may affect the coating surface, it will lead to unevenness rather than micron scale roughness and only contribute marginally to ice formation on the surface.

The influence of surface roughening on the measured water freezing temperature, as shown in Fig. 5, is minimal. However, roughening of the test surfaces did increase the measured receding water contact angle (Table 2) as anticipated by the known relationship between these properties,[61] suggesting that surface roughness has the

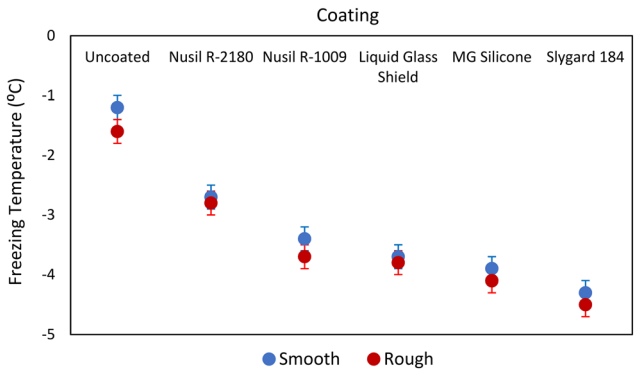

Fig. 5 Freezing temperature comparison for a 150 μL water droplet on smooth and rough AA 2024-T3.

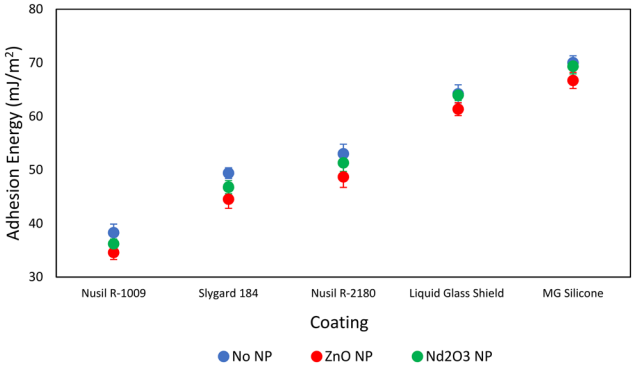

Fig. 6 Comparison of estimated adhesion energies of a 150 μL water droplet on various coatings with added ZnO and Nd_2O_3 nanoparticles on smooth AA 2024-T3 coupons.

potential to endow the substrate with better anti-icing properties. Hydrophobic and anti-icing characteristics can be imparted to free surfaces by surface texturing, roughening, patterning, or application of micro- or nano-particles.[70] However, the actual function of roughened surfaces is affected by the scale and the environment. The micro-scaled roughness lowers the ice adhesion strength, while the nano-scale texture resists droplet impingement and promotes rebound.[71] Hence, the ice adhesion strength generally decreases as the water contact increases. However, when the atmospheric humidity level is high, water on the roughened/textured surface can change from a Cassie–Baxter state with trapped air below the water droplet to a Wenzel state, reducing in fact the contact angles (<90°). As a result, surface roughening strategies for anti-icing purposes must be designed according to the application environment and durability of the textured surface. In this regard, application of particulates to the surface has the advantage of unrestricted particle size, has the ability of periodical re-application and does not affect the mechanical integrity of the underlying substrate.

Influence of ZnO and Nd_2O_3 nanoparticles on delayed ice formation

The presence of ZnO and Nd_2O_3 nanoparticles on bare AA 2024-T3 coupons and in coatings was found to reduce the water freezing temperature on all smooth/roughened samples (Fig. 4). Surfaces modified with ZnO nanoparticles consistently demonstrated the greatest decrease in water freezing temperature, followed by those with Nd_2O_3 nanoparticles. ZnO nanoparticles, nanorods, and nanohairs had previously been incorporated into several coatings where they were found to increase the anti-icing properties. This functionality was particularly observed on surfaces where ZnO nanoparticles were secured to silicone substrates through ZnO–Si_2O bonds.[72] As the majority of coatings used in this study are silicone-based, similar anti-icing behaviour was observed on these modified coupons. Interestingly, comparably lower temperatures of water freezing were

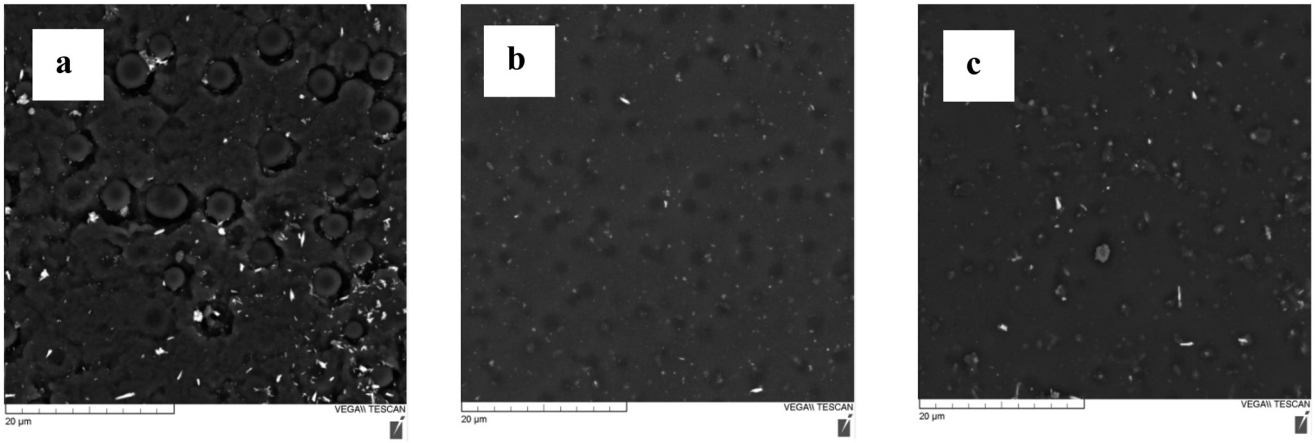

Fig. 7 SEM images of test samples coated with Nusil® R-1009 prepared with and without the following nanoparticles: (a) no nanoparticles, (b) ZnO, and (c) Nd_2O_3.

similarly observed on the silicone-free coating (Liquid Glass Shield) suggesting that these different surface interactions between ZnO nanoparticles and silicone-free coatings were not the major factor responsible for lowering the freezing temperature. In turn, Nd_2O_3 nanoparticles are a known rare-earth oxide with a strong intrinsic hydrophobicity.[73] It was proposed that this surface property may lower the temperature of water freezing due to the relationship between hydrophobicity and icephobicity. Given the observed decrease in water freezing temperature on Nd_2O_3 nanoparticle-coated surfaces, it was concluded that Nd_2O_3 nanoparticles also enhance the icephobicity of the selected coatings though not necessarily to the same degree as ZnO nanoparticles.

Influence of ZnO and Nd_2O_3 nanoparticles on surface energy

Surface energy heavily influences the temperature at which ice forms on a solid surface. Surfaces with lower surface energies typically favor supercooling of water and a decreased surface temperature at water freezing. As the change in surface roughness within each set of coating was negligible, changes in surface energy among coated samples with added metal oxide nanoparticles could have contributed to a decrease in the water freezing temperatures.

The free energy of solids can be determined using Young's equation which establishes a relationship between contact angle measurements, liquid surface tension, and interfacial tension between the liquid and solid as shown in eqn (1):

$$\sigma_{SG} = \sigma_{SL} + \sigma_{LG}\cdot\cos\theta \quad (1)$$

where σ_{SG} is the surface free energy of the solid, σ_{SL} is interfacial tension between the solid and liquid, σ_{LG} is the surface tension of the liquid, and θ is the contact angle.

In cases of partial wetting by water droplets, this relation can be simplified to the Young–Dupré equation (eqn (2)):

$$W_{SL} = \gamma_L(1 + \cos\theta) \quad (2)$$

where W_{SL} is the adhesion energy, γ_L is the surface tension, and θ is the measured water contact angle.

A comparison of adhesion energies for each coating, with and without added nanoparticles, estimated using the water/air surface tension at 0 °C and the measured contact angles are demonstrated in Fig. 6. The addition of these metal oxide nanoparticles to the coatings was found to lower the estimated adhesion energy. This decrease was most pronounced in coatings containing ZnO nanoparticles (4.83–2.86 mJ m^{-2} difference). However, Nd_2O_3 nanoparticle coupons also showed a slight decrease in adhesion energy (2.09–0.25 mJ m^{-2} difference) among different coatings. Given the correlation between lower surface energies and reduced ice adhesion, these results support the observed decrease in water freezing temperatures for coatings with metal oxide nanoparticles. Further knowledge of the surface distribution pattern and intrinsic surface properties of ZnO and Nd_2O_3 is required for more precise surface energy calculations. As such, scanning electron microscopy (SEM) images were collected to verify these findings.

Influence of ZnO and Nd_2O_3 nanoparticles on surface morphology

SEM images were collected using a Tescan Vega-II XMU SEM to illustrate the morphology of the test surfaces and the distribution of metal oxide nanoparticles within the coatings. The addition of both ZnO and Nd_2O_3 nanoparticles was shown to decrease the number of surface asperities and contribute to the smoothing of the coating (Fig. 7). The uneven distribution of asperities on the coating surface does not reflect the precise micro- or nano-scale patterning used to suspend water droplets above the surface in the Cassie–Baxter model and increase icephobicity. As such, the surface leveling modification induced by the ZnO and Nd_2O_3 nanoparticles is expected to reduce ice nucleation, which is

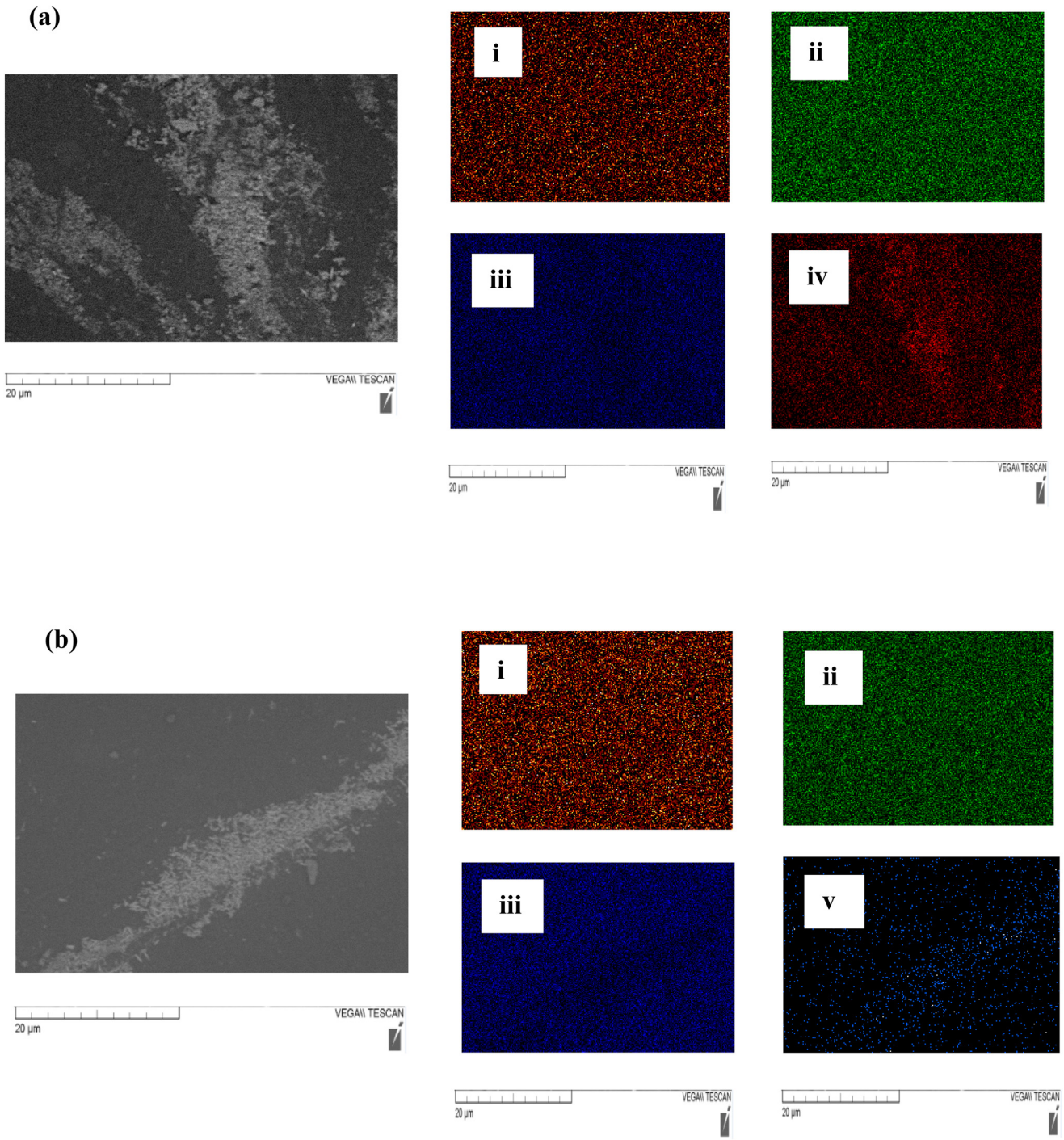

Fig. 8 Surface mapping of the following elements on coating surfaces with added (a) ZnO and (b) Nd_2O_3 nanoparticles: (i) carbon, (ii) oxygen, (iii) silicon, (iv) zinc, and (v) neodymium.

an anti-icing property indicative of lower surface energy. As such, the SEM images support the adhesion energy trends observed in the above estimations.

Oxford Inca Energy X-Act electron dispersive spectrometry software was also used to conduct elemental mapping of the SEM images. As shown in Fig. 8, elemental analysis was used to verify nanoparticle distribution within the coating. The silicone coatings (Nusil® R-1009, Nusil® R-2180, Sylgard 184 and MG Silicone) have chemical compositions consisting of carbon, oxygen and silicon. Therefore, it was unsurprising to observe an even distribution of these compounds across the full test surface. The SEM imaging of the coatings also showed instances of aggregation for both ZnO and Nd_2O_3 nanoparticles on the surface, as verified by elemental mapping of greater concentrations of zinc and neodymium in select areas. These findings indicate that the nanoparticles

did not maintain perfectly uniform distribution across the surface due to aggregation.[74] However, the signals for both zinc and neodymium were still detected throughout the coatings illustrating full nanoparticle coverage across the surface despite this clustering. The signal for oxygen in Fig. 8(a)ii and (b)ii reminds us of the fact that metal oxide nanoparticles have very different chemical compositions, physical properties (solubility), and toxicity (production of reactive oxygen species) than metal nanoparticles (with no oxide) or carbon-based nanoparticles (with no metal or oxide).[75]

There are many methods that can play a passive role in rendering the anti-icing features to the surface or to the water/fluid itself in terms of reducing ice formation temperature and/or delaying the nucleation of ice.[76] One of these methods is the addition of nano- or micro-particulates to the surface or to the fluid. However, the nature of these particulates (barrier to ice formation, diameter, aspect ratio, size distribution and concentration) must be carefully examined and controlled under an applicable environment to avoid the potential increase in ice formation temperature.[77] To this effect, a study with a coating of nano sized VO_2/PDMS (estimated to be 100 nm in diameter) has resulted in water contact angle increase, ice adhesion reduction and delay in icing.[78] It has also theorized that a surface with a high water contact angle will allow the accumulated ice on the surface to be removed with much less force, such as wind or aerodynamic force during operation of aircrafts or wind turbines. The excellent anti-icing performance of a superhydrophobic coating surface of ZnO on aluminum alloy,[76] ZnO on stainless steel substrates,[77] ZnO on fluorinated organic coatings,[78] ZnO/polydimethylsiloxane composite,[79] ZnO/CuS composite,[80] and ZnO/MoS_2 nano-coatings[81] had previously been presented. On the contrary, no anti-icing performance of Nd_2O_3 had been reported in the scientific literature. Hence, its weak performance was expected when Nd_2O_3 nanoparticles were used as a negative control for testing cyclic voltammetry in the present work. The crystalline phase of Nd_2O_3 nanoparticles was determined by XRD as a hexagonal simple basic structure (lattice parameters: $a \approx 3.85$ Å, $c \approx 6.10$ Å), which is similar to the hexagonal wurtzite structure ($a \approx 3.25$ Å, $c \approx 5.20$ Å) reported for ZnO nanoparticles.[82–88] However, ZnO and Nd_2O_3 differ significantly in their physicochemical properties that can influence their anti-icing performance. For instance, ZnO has high thermal conductivity (50–60 W m^{-1} K^{-1}) and the thermal conductivity of Nd_2O_3 is lower. Last, ZnO is an intrinsic n-type semiconductor with good electron mobility, whereas Nd_2O_3 is an insulator. Further investigation will be required to clarify the weak anti-icing performance of Nd_2O_3 nanoparticles.

Conclusion

This study applied cyclic voltammetry as an electrochemical analysis technique to detect ice formation on AA 2024-T3 coupons with a variety of commercially available icephobic coatings. A reduction in surface temperature at ice formation was observed across all the coated samples. The coupon test surfaces were further roughened by sand blasting with alumina or modified by adding ZnO and Nd_2O_3 nanoparticles to the coatings. Coupons with roughened surfaces showed only marginal increases in hydrophobicity as determined by their measured water contact angles. This finding was attributed to the self-leveling properties of the liquid coatings which smoothened out the surface particularly in cases where the coating thickness was greater than the surface roughness profile. On the contrary, surfaces with ZnO and Nd_2O_3 nanoparticles added to the coatings were found to exhibit an increased reduction of temperature at water freezing due to lowered surface energy. These shifts in surface temperature at water freezing demonstrate better anti-icing properties as a result of the surface modification. More importantly, a methodology based on cyclic voltammetry was established as an electrochemical analysis tool that can have wider application in service to detect ice formation on airframe surfaces.

Data availability

The data supporting this article have been included as part of the ESI.†

Conflicts of interest

The authors declare that they have no known competing financial interests or personal relationships that could have appeared to influence the work reported in this paper. This manuscript is compiled from a M.Sc. thesis of the first author.

Acknowledgements

This research was supported by the Aerospace Future Initiative Program (A1-018251) of the National Research Council Canada.

References

1 F. T. Lynch and A. Khodadoust, *Prog. Aerosp. Sci.*, 2001, **37**, 669–767.
2 W. A. Cooper, W. R. Sand, M. K. Politovich and D. L. Veal, *J. Aircr.*, 1984, **21**, 708–715.
3 M. B. Bragg, A. P. Broeren and L. A. Blumenthal, *Prog. Aerosp. Sci.*, 2005, **41**, 323–362.
4 A. Azimi Yancheshme, G. Momen and R. Jafari Aminabadi, *Adv. Colloid Interface Sci.*, 2020, **279**, 102155.
5 Y. Cao, Z. Wu, Y. Su and Z. Xu, *Prog. Aerosp. Sci.*, 2015, **74**, 62–80.
6 M. K. Politovich, *J. Aircr.*, 2003, **40**, 639–644.
7 M. K. Politovich, *J. Appl. Meteorol.*, 1989, **28**, 856–868.
8 W. Huang, J. Huang, Z. Guo and W. Liu, *Adv. Colloid Interface Sci.*, 2022, **304**, 102658.

9 Y. Shen, X. Wu, J. Tao, C. Zhu, Y. Lai and Z. Chen, *Prog. Mater. Sci.*, 2019, **103**, 509–557.
10 R. Menini, Z. Ghalmi and M. Farzaneh, *Cold Reg. Sci. Technol.*, 2011, **65**, 65–69.
11 C. Laforte, C. Blackburn and J. Perron, in *SAE Technical Paper Series*, SAE International, 400 Commonwealth Drive, Warrendale, PA, United States, 2015.
12 P. Irajizad, S. Nazifi and H. Ghasemi, *Adv. Colloid Interface Sci.*, 2019, **269**, 203–218.
13 M. Grizen and M. K. Tiwari, *Ice Adhes.*, 2020, 417–466.
14 H. Sojoudi, M. Wang, N. D. Boscher, G. H. McKinley and K. K. Gleason, *Soft Matter*, 2016, **12**, 1938–1963.
15 F. Piscitelli, A. Chiariello, D. Dabkowski, G. Corraro, F. Marra and L. Di Palma, *Aerospace*, 2020, **7**, 2.
16 S. Farhadi, M. Farzaneh and S. A. Kulinich, *Appl. Surf. Sci.*, 2011, **257**, 6264–6269.
17 Y. Lin, H. Chen, G. Wang and A. Liu, *Coatings*, 2018, **8**, 208.
18 J. T. Simpson, S. R. Hunter and T. Aytug, *Rep. Prog. Phys.*, 2015, **78**, 086501.
19 T.-S. Wong, S. H. Kang, S. K. Y. Tang, E. J. Smythe, B. D. Hatton, A. Grinthal and J. Aizenberg, *Nature*, 2011, **477**, 443–447.
20 A. Lafuma and D. Quéré, *EPL*, 2011, **96**, 56001.
21 D. Chen, M. D. Gelenter, M. Hong, R. E. Cohen and G. H. McKinley, *ACS Appl. Mater. Interfaces*, 2017, **9**, 4202–4214.
22 E. Farahani, A. C. Liberati, A. Mahdavi, P. Stoyanov, C. Moreau and A. Dolatabadi, *Coatings*, 2023, **13**, 1049.
23 M. Nosonovsky and V. Hejazi, *ACS Nano*, 2012, **6**, 8488–8491.
24 W. Hou, Y. Shen, J. Tao, Y. Xu, J. Jiang, H. Chen and Z. Jia, *Colloids Surf., A*, 2020, **586**, 124180.
25 H. Saito, K. Takai and G. Yamauchi, *Surf. Coat. Int.*, 1997, **80**, 168–171.
26 R. Attarzadeh and A. Dolatabadi, *Int. J. Heat Mass Transfer*, 2019, **136**, 1327–1337.
27 H. Gao, Y. Jian and Y. Yan, *Soft Matter*, 2021, **17**, 447–466.
28 L. Cao, A. K. Jones, V. K. Sikka, J. Wu and D. Gao, *Langmuir*, 2009, **25**, 12444–12448.
29 E. Bakhshandeh, S. Sobhani, R. Jafari and G. Momen, *J. Appl. Polym. Sci.*, 2023, **140**, e54610.
30 L. Zhao, Y. Shen, W. Liu, J. Tao and S. Liu, *Surf. Interfaces*, 2023, **42**, 103510.
31 L. Haworth, D. Yang, P. Agrawal, H. Torun, X. Hou, G. McHale and Y. Fu, *Nanotechnol. Precis. Eng.*, 2023, **6**, 013007.
32 L.-B. Zhang, H.-X. Zhang, Z.-J. Liu, X.-Y. Jiang, S. Agathopoulos, Z. Deng, H.-Y. Gao, L. Zhang, H.-P. Lu, L.-J. Deng and L.-J. Yin, *J. Colloid Interface Sci.*, 2023, **630**, 1–10.
33 O. Redondo, S. G. Prolongo, M. Campo, C. Sbarufatti and M. Giglio, *Compos. Sci. Technol.*, 2018, **164**, 65–73.
34 N. Karim, M. Zhang, S. Afroj, V. Koncherry, P. Potluri and K. S. Novoselov, *RSC Adv.*, 2018, **8**, 16815–16823.
35 O. Gohardani, M. C. Elola and C. Elizetxea, *Prog. Aerosp. Sci.*, 2014, **70**, 42–68.
36 J. Liu, Z. Janjua, M. Roe, F. Xu, B. Turnbull, K.-S. Choi and X. Hou, *Nanomaterials*, 2016, **6**, 232.
37 S. Pathak, G. C. Saha, M. B. Abdul Hadi and N. K. Jain, *Coatings*, 2021, **11**, 382.
38 M. A. Kulkarni, A. Yengantiwar, M. Deo and A. G. Banpurkar, *Mater. Sci. Eng., B*, 2022, **285**, 115969.
39 M. Cappadonia, S. Krause and U. Stimming, *Electrochim. Acta*, 1997, **42**, 841–848.
40 J. O. Bockris and J. Wass, *J. Electroanal. Chem. Interfacial Electrochem.*, 1989, **267**, 325–327.
41 A. M. Bond and L. Zongpeng, *J. Electroanal. Chem. Interfacial Electrochem.*, 1989, **259**, 189–205.
42 A. M. Bond, M. Fleischmann and J. Robinson, *J. Electroanal. Chem. Interfacial Electrochem.*, 1984, **168**, 299–312.
43 A. M. Bond and V. B. Pfund, *J. Electroanal. Chem.*, 1992, **335**, 281–295.
44 V. Tsionsky, E. Alengoz, L. Daikhin, A. Kaverin, D. Zagidulin and E. Gileadi, *Electrochim. Acta*, 2005, **50**, 4212–4221.
45 D. K. Gosser and Q. Huang, *J. Electroanal. Chem. Interfacial Electrochem.*, 1989, **267**, 333–338.
46 D. K. Gosser Jr. and Q. Huang, *J. Electroanal. Chem. Interfacial Electrochem.*, 1990, **278**, 399–402.
47 D. K. Gosser Jr., Q. Huang and P. H. Rieger, *J. Electroanal. Chem. Interfacial Electrochem.*, 1990, **286**, 285–289.
48 K. Yeadon, E. P. C. Lai, N. Song and X. Huang, *Langmuir*, 2023, **39**, 17644–17652.
49 D. G. Jackson and J. I. Goldberg, in *SAE Technical Paper Series*, SAE International, 400 Commonwealth Drive, Warrendale, PA, United States, 2007.
50 0871TD Series General Aviation Ice Detector, **https://www.collinsaerospace.com/what-we-do/industries/business-aviation/exteriors/ice-detection-systems/affordable-ice-detection**, (accessed July 18, 2024).
51 New Avionics Corporation, IceMeisterTM Model 9732-STEEL.
52 NF.0075-1120 Lucas MK.3B Aerospace Ice Detector (Core), **https://baspartsales.com/nf-0075-1120-lucas-mk-3b-aerospace-ice-detector/**, (accessed July 18, 2024).
53 Avantor, **https://nusil.avantorsciences.com/nusil/en/product/R-1009/rtv-silicone-coating**, (accessed July 18, 2024).
54 Avantor, **https://nusil.avantorsciences.com/nusil/en/product/R-2180/ice-phobic-coating**, (accessed July 18, 2024).
55 Liquid Glass Shield, Product information sheet, **https://liquidglassshield.com/wp-content/uploads/2020/06/LGS-Automotive-Data-Sheet.pdf**.
56 MG Chemicals, *422B: Safety Data Sheet*, 2020.
57 SYLGARD 184 Silicone Elastomer Kit, **https://www.dow.com/en-us/pdp.sylgard-184-silicone-elastomer-kit.01064291z.html#overview**, (accessed July 18, 2024).
58 ramé-hart DROPimage Family of Software, **https://www.ramehart.com/dropimage.htm**, (accessed July 20, 2024).
59 A. J. Meuler, J. D. Smith, K. K. Varanasi, J. M. Mabry, G. H. McKinley and R. E. Cohen, *ACS Appl. Mater. Interfaces*, 2010, **2**, 3100–3110.
60 R. N. Wenzel, *J. Phys. Colloid Chem.*, 1949, **53**, 1466–1467.
61 C. Li, J. Zhang, J. Han and B. Yao, *Sci. Rep.*, 2021, **11**, 459.
62 J. P. Youngblood and N. R. Sottos, *MRS Bull.*, 2008, **33**, 732–741.

63 G. Heydari, E. Thormann, M. Järn, E. Tyrode and P. M. Claesson, *J. Phys. Chem. C*, 2013, **117**, 21752–21762.
64 M. He, J. Wang, H. Li and Y. Song, *Soft Matter*, 2011, **7**, 3993.
65 M. Wang, W. Yu, Y. Zhang, J.-Y. Woo, Y. Chen, B. Wang, Y. Yun, G. Liu, J. K. Lee and L. Wang, *J. Ind. Eng. Chem.*, 2018, **62**, 52–57.
66 H. AlMohamadi and K. J. Smith, *Catalysts*, 2019, **9**, 557.
67 G. Azimi, R. Dhiman, H.-M. Kwon, A. T. Paxson and K. K. Varanasi, *Nat. Mater.*, 2013, **12**, 315–320.
68 S. Jung, M. Dorrestijn, D. Raps, A. Das, C. M. Megaridis and D. Poulikakos, *Langmuir*, 2011, **27**, 3059–3066.
69 S. Chang, H. Qi, S. Zhou and Y. Yang, *Appl. Therm. Eng.*, 2023, **219**, 119516.
70 X. Huang, N. Tepylo, V. Pommier-Budinger, M. Budinger, E. Bonaccurso, P. Villedieu and L. Bennani, *Prog. Aerosp. Sci.*, 2019, **105**, 74–97.
71 T. M. Schutzius, S. Jung, T. Maitra, P. Eberle, C. Antonini, C. Stamatopoulos and D. Poulikakos, *Langmuir*, 2015, **31**, 4807–4821.
72 H. He and Z. Guo, *iScience*, 2021, **24**, 103357.
73 G. Carchini, M. García-Melchor, Z. Łodziana and N. López, *ACS Appl. Mater. Interfaces*, 2015, **8**, 152–160.
74 Y. Xiong, X. Liu and H. Xiong, *Sci. Rep.*, 2021, **11**, 17386.
75 A. B. Sengul and E. Asmatulu, *Environ. Chem. Lett.*, 2020, **18**, 1659–1683.
76 G. Bai, D. Gao, Z. Liu, X. Zhou and J. Wang, *Nature*, 2019, **576**, 437–441.
77 J. Liu, C. Zhu, K. Liu, Y. Jiang, Y. Song, J. S. Francisco, X. C. Zeng and J. Wang, *Proc. Natl. Acad. Sci. U. S. A.*, 2017, **114**, 11285–11290.
78 Y. Liu, R. Sun, B. Jin, T. Li, L. Yao, L. Feng and J. He, *ACS Appl. Nano Mater.*, 2022, **5**, 5599–5608.
79 G. Liu, Y. Yuan, Z. Jiang, J. Youdong and W. Liang, *Mater. Res. Express*, 2020, **7**, 026401.
80 Y. Deng, F. Xu, Z. Yin, M. Xue, Y. Chen, P. He, J. Wu, J. Ou, F. Wang, Y. Luo and Z. Hong, *Ceram. Int.*, 2023, **49**, 25135–25143.
81 Z. Zeng, J. He, J. Jie, C. Zhou, B. Chen, J. Bao, K. Yang and J. Luo, *Mater. Res. Express*, 2021, **8**, 115008.
82 C. Yang, F. Wang, W. Li, J. Ou, C. Li and A. Amirfazli, *Appl. Phys. A: Mater. Sci. Process.*, 2016, **122**, 1.
83 Y. Bao, H. Yang, L. Gao, X. Zheng, X. Shi, W. Zhang and C. Liu, *Sol. Energy Mater. Sol. Cells*, 2022, **245**, 111838.
84 B. Liu, Z. Liu, Y. Li and F. Feng, *Coatings*, 2023, **13**, 686.
85 W. Bousslama, H. Elhouichet, B. Gelloz, B. Sieber, A. Addad, M. Moreau, M. Férid and N. Koshida, *Jpn. J. Appl. Phys.*, 2012, **51**, 04DG13.
86 P. Bindu and S. Thomas, *J. Theor. Appl. Phys.*, 2014, **8**, 123–134.
87 M. Kahouli, A. Barhoumi, A. Bouzid, A. Al-Hajry and S. Guermazi, *Superlattices Microstruct.*, 2015, **85**, 7–23.
88 M. A. Ismail, K. K. Taha, A. Modwi and L. Khezami, *J. Ovonic Res.*, 2018, **14**, 381–393.